Structure and Ion Transport of Lithium-rich $Li_{1+x}Al_xTi_{2-x}(PO_4)_3$ with 0.3<x<0.5: A Combined Computational and Experimental Study[†]

David Case[a], Adam J. McSloy[a], Ryan Sharpe[a], Stephen R. Yeandel[a], Thomas Bartlett[b], James Cookson[b], Enkhe Dashjav[c], Frank Tietz[c,d], C. M. Naveen Kumar[e,f,#], Pooja Goddard*[a]

New solid state electrolytes are becoming increasingly sought after in the drive to replace flammable liquid electrolytes. To this end, several Li conducting solids have been identified as promising candidates including Li stuffed garnets and more recently Li-rich materials such as $Li_{1+x}Al_xTi_{2-x}(PO_4)_3$ with 0.3<x<0.5. However, the structure/property relationships of LATP are incredibly sensitive to synthesis conditions and therefore challenging to optimise. In this joint computational and experimental investigation, we examine the structural sensitivities by modelling the site occupancies at varying temperature, which clarifies previously reported discrepancies of the crystal structures. Furthermore, we investigate the Li ion transport properties which have not reported computationally before. We confirm from our simulations that the migration pathway only involves the M1(6b) and M2(18e) site, in excellent agreement with the neutron diffraction data, clarifying all past controversies regarding the Li ion occupancies in LATP. Interestingly, we calculate low migration barriers (0.3eV) in line with experimental findings but also show evidence of Li ion trapping on Al doping in LATP (where x=0.4), possibly explaining the experimental observation that the Li ion conductivity does not improve above x=0.3, due to a stronger repulsion between Li^+–>Ti^{4+} compared to Li^+–>Al^{3+}. Furthermore, our calculated ionic conductivities are in excellent agreement with experimental values, highlighting the robustness of our computational models.

1 Introduction

Li-ion batteries have been very successful in the small portable electronics market, however safety concerns and the desire to replace the flammable liquid electrolytes currently used have limited their commercialization as large scale grid storage applications. The use of a solid state electrolyte in a lithium battery is a promising alternative that would address the concerns over safety and energy density. To this end, $Li_{1+x}Al_xTi_{2-x}(PO_4)_3$, henceforth referred to as LATP, has been reported with encouraging bulk properties; for example its electrochemical window of 2.4 V[1] and stability versus water,[2] coupled to its encouraging lithium ion conductivity (between 10^{-4} and 10^{-3} S cm^{-1}),[3,4] make it one of the most promising candidates under consideration for the the next generation of all-solid-state lithium ion batteries.

LATP crystallizes in the NASICON-type structure with space group $R\bar{3}c$.[5] The structure is derived from $LiTi_2(PO_4)_3$ (henceforth referred to as LTP), where x Al^{3+} ions replace x Ti^{4+} ions. This allows an additional x Li^+ ions to be added to the structure, thereby increasing the lithium concentration relative to the LTP structure. The positions of the extra lithium ions is not trivial as common characterization techniques such as X-ray diffraction and neutron diffraction have shown varying sites of the Li^+ ions and different site occupancies leading to the assumption that the Li ion distribution in the NASICON lattice depends on the thermal history of the material.[6]

Dashjav and Tietz[7] reported an LATP structure in which the Li1 site (labeled M1), with fractional coordinates (0,0,0) and Wyckoff symbol 6b, is fully occupied. The M2(18e) site at (0.64525, 0, 0.25), proposed to be a bridging site between the M1(6b) sites has also been reported.[8] However the structure of Dashjav and Tietz showed that the additional x lithium ions reside in a M1$'$(6a) site

---

[a] Department of Chemistry, Loughborough University, Loughborough LE11 3TU, United Kingdom.

[b] Johnson Matthey Technology Centre, Blounts Court Road, Sonning Common, Reading RG4 9NH, United Kingdom.

[c] Forschungszentrum Jülich GmbH, Institute of Energy and Climate Research (IEK-1), 52425 Jülich, Germany.

[d] Helmholtz-Institute Münster, Forschungszentrum Jülich GmbH, 52425 Jülich, Germany.

[e] Forschungszentrum Jülich GmbH, Jülich Centre for Neutron Science (JCNS), Outstation at SNS, Oak Ridge National Laboratory, Oak Ridge, Tennessee 37831, USA.

[f] Chemical and Engineering Materials Division, Oak Ridge National Laboratory, Oak Ridge, Tennessee 37831, USA.

[#] new address: Vienna University of Technology, Institute of Solid State Physics, Wiedner Hauptstr. 8, 1040 Wien, Austria.

located at (0, 0, 0.25). The final site that has been discussed in the literature is the M3(36f) site at (0.63667, 0.01333, 0.27333),[9] which lie on either side of the M2(18e) positions, and therefore have been considered equivalent to the M2(18e), shown in figure 1. Additional lithium (above $x = 0.3$) can be incorporated on the M2(18e) site,[7] but the space group changes to $R\bar{3}$.[10] The lithium conductivity is known to increase markedly as x is increased from 0.0, exhibiting a maximum when $0.3<x<0.5$,[11–13] indicating a dependence on materials processing and hence materials quality due to a significant impact of the grain boundaries on the total conductivity.[14] As a comparison, the maximum bulk conductivity was found at $x = 0.4$ measured on single crystals.[15]

Previous work on the mechanism of lithium diffusion in LATP has used techniques such as X-ray and neutron diffraction,[9,10] impedance spectroscopy and ^{7}Li NMR.[16] Arbi *et al.*[10] compare this data to that which would be predicted from the difference bond valence analysis, and conclude that the Li diffuses with local minima at the M3(36f) sites, and has a total barrier of 0.33 eV, in excellent agreement with our modelling results discussed further on in the paper. Arbi *et al.*[10] also deduced the structure of LATP from neutron diffraction and performed ^{7}Li NMR at different temperatures to observe that Li is diffusing, but did not calculate explicit numbers. However,the same group previously used NMR and impedance spectroscopy[16] and reported that substitution of LTP with Al greatly increases Li diffusion, ascribing this to M1(6b) site occupancies.

Earlier computational studies, using Density Functional Theory (DFT) to calculate diffusion barriers and the influence of substitutions of titanium atoms, calculated an activation energy barrier for Li vacancy diffusion of 0.41 eV in LTP, and by including an extra Li ion, an interstitial migration barrier of 0.19 eV.[8] However, it was also reported that Li is trapped by the introduction of Al dopants.[8]

Nuspl *et al.*[17] performed molecular dynamics calculations on this material and observed Li ions moving to new sites within the first 100 ps. Using the Connolly surface analysis the authors see a typical pathway with an energy barrier between M1 and M2 sites of around 0.3 eV.

In this joint computational and experimental paper we study the crystal structure, and clarify the Li ion positions with respect to sensitivities to synthesis conditions, which have been controversial in the literature. More importantly the computational studies elucidate the Li ion diffusion, in particular the migration pathways and barriers. All of which corroborate exceptionally with observed experimental data.

2 Methodology

2.1 Computational Modelling

Interatomic potential calculations were based on the Born model of ionic solids where long and short-range pairwise terms are used to describe the Coulombic, Pauli repulsive and Van der Waals interactions. In this study, the short-range Buckingham potential was employed:[18]

$$\Phi_{ij}(r) = A\,\exp\left(-\frac{r}{\rho}\right) - \frac{C}{r^6} \qquad (1)$$

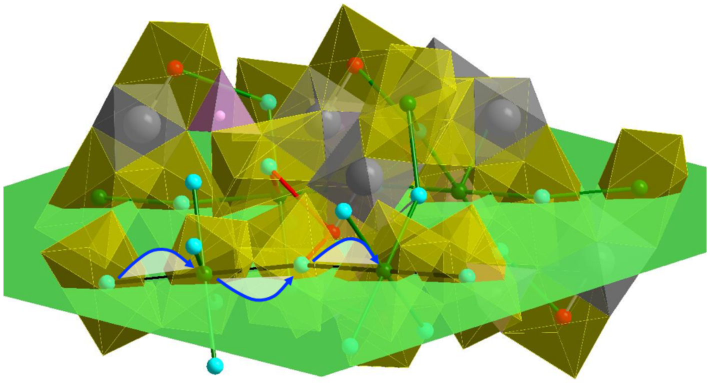

Fig. 1 Schematic slice of the LATP crystal structure for visualisation of conduction paths. The LiO_6 polyhedra are shown in yellow, the PO_4 tetrahedra in purple and the $(Ti,Al)O_6$ octahedra in grey. Three different atomic sites for Li atoms are shown as green, red and cyan for M1 (6b), M1$'$ (6a) and M2 (18e) sites, respectively. Thick green and black lines indicate two parallel running zig-zag chains of -M1-M2-M1- connection paths, which are lying on the (114) plane (shown in light green). The real conduction path has an S-shaped curvature as indicated by the blue arrows. It is worth noting that LATP measured at 573 K only has M1 and M2 Li sites occupied, whereas LATP measured at 298 K shows occupancy of all three different Li sites. The M1 site, also located within the (114) plane, is connected with two M2 sites here accentuated as red sticks and resulting in a conduction path M2-M1-M2-M1 by combining Li sites from higher and lower lying parallel planes. The shorter interatomic distance of 3.11 Å of M1-M2 is obviously more favorable for the Li conduction than that of 3.42 Å of M1-M2

In this equation, Φ_{ij} is the Buckingham potential energy emanating from the interaction of ions i and j at a distance r. The terms A, ρ and C are the interaction specific potential parameters. Buckingham interactions were omitted for cation-cation interactions in this work. Oxide ion polarizability was included using the Dick and Overhauser shell model.[19] Interatomic potential based (PB) static lattice calculations in this work were conducted using the General Utility Lattice Program (GULP).[20,21] These methods have been commonly employed to investigate ceramic materials, numerous examples of which can be found in literature. The phosphate potential was taken from Islam *et al.*[22] and its Buckingham terms were fixed, as were the partial charge and spring constant for the oxygen shell model. The phosphate model was simplified, with no measured loss in accuracy, by removing its shell and three-body terms. This model was selected as it has been previously used to study the common cathode material $LiFePO_4$.[23]

To derive parameters for the remaining interactions, a quasi-random Sobel sequence based search was conducted.[24] In a typical run, tens of thousands of parameters were calculated, the structures optimised and ranked according to a metric based on reproducing experimental or DFT optimised bond and unit cell lengths. The best parameters were re-optimised with a simplex algorithm. This routine generates parameters for the Ti^{4+}–O^{2-}, Li^{+}–O^{2-}, O^{2-}–O^{2-} interactions by fitting to LTP.[25] This was supplemented by an Al^{3+}–O^{2-} potential by fitting to Al_2TiO_5.[26] As Al_2TiO_5 is a disordered structure, the fit was measured with respect to two configurations which had been optimised with DFT (using the PBE functional) *via* the VASP program.[27] These potentials optimise the structures to stable minima, with positive phonons, and are also valid for common binary oxides of aluminium and titanium. Differences in the unit cell and bond lengths along with details of the DFT calculations are given in the supplementary material. The final interatomic potential model is presented in table 1.

Table 1 The interatomic Buckingham potentials used in this work. All interactions are through the shell particle of oxygen, which has a charge of -2.86 atomic units, and is coupled to the core *via* a harmonic spring with a force constant of 65.0 eV Å^{-1}.

Species	A (eV)	ρ (Å)	C_6 (eV Å^6)
O^{2-}–O^{2-}	12759.2067	0.2174	29.9751
P^{5+}–O^{2-}	897.2648	0.3577	0.0
Li^{+}–O^{2-}	970.8187	0.2663	0.0
Ti^{4+}–O^{2-}	6622.3671	0.2545	0.0
Al^{3+}–O^{2-}	1761.2076	0.2922	0.0

The interatomic Buckingham potentials selected to model LATP in this work (listed in Table 1) produce an acceptable fit (within 2 %) to the previous experimentally determined structures,[7] as well as the refined structures reported in this work, see supplementary information for full experimental structures.

A comparison of the experimental and calculated LATP structures are listed in table 2. Our interatomic potentials yield elastic modulus between 74-104 GPa. Our experimentally measured elastic modulus ranges from 70 - 100 GPa, depending on the density of the samples. In comparision to experimental elastic modulus reported in the literature 81-115 GPa.[?] As our caluclated elastic moduli are within both our measured experimental range and literatures, this strengthens the confidence in our interatomic potential model. Furthermore, the interatomic potentials also yield models that are in good agreement with the experimentally determined structures for $Li_4Ti_5O_{12}$,[28] Al_2TiO_5[26] and LTP,[25] see supplementary information for details. The transferable nature exhibited by the selected potential model, listed in table 1 strengthens the justification for its choice.

Classical Molecular dynamic (MD) simulations using the interatomic potentials discussed above were performed using DL_POLY classic[29] on three $5\times5\times2$ supercell configurations, each containing 5522 atoms. Each configuration's structure was based on that reported by Dashjav and Tietz[7]. Al↔Ti substitutions and Li insertion sites were selected according to a Sobol quasi-random number sequence.[24] Systems were equilibrated at zero Kelvin to remove any excess energy before simulating using an isobaric-isothermal ensemble (NPT, where the temperature and stress applied were kept constant). The Berendsen thermostat was used with a 0.2 ps relaxation time, to permit thermal expansion. Final production runs were carried out using a canonical ensemble (NVT, where the temperature and volume were fixed) at a pressure of 1.0 atm for 3.0 ns using the Nosé-Hoover (0.5 ps relaxation time) thermostat with a time-step of 0.5 fs and a 50 ps equilibration period. Five target temperatures, from 273 to 573 K in steps of 75 K were simulated, in each the trajectory snapshots were written every 0.5 ps. All simulations used the Verlet-Leapfrog integrator and an 12 Å short range force cutoff.

In order to quantify the displacement of lithium ions over time, the diffusion coefficients (D) were calculated from the mean squared displacements (MSD, $\langle[\Delta\vec{r}(t)]^2\rangle$) *via* equation 2 using a module from the PyMatGen package.[30]

$$D = \frac{\mathrm{MSD}}{6t} \tag{2}$$

The occupancies of the Li sites were calculated by assigning each Li^{+} ion to its nearest site of relevant type, averaging over snapshots taken every 0.5 ps. This was made computationally tractable by using the k-d tree algorithm in the package scikit-learn.[31]

2.2 Experimental

LATPx samples with x = 0.3, 0.4, and 0.5 were prepared by a sol-gel method described previously.[12,32] Neutron powder diffraction (ND) measurements were performed on the time-of-flight (TOF) powder diffractometer, POWGEN, located at the Spallation Neutron Source at Oak Ridge National Laboratory. The data were collected with neutrons of central wavelengths 1.333 Å and 2.665 Å covering the d-spacing range of 0.45-6.2 Å and 1.15-10.5 Å, respectively. For the ND measurements, approximately 2 g of each sample was loaded in a vanadium can of 10 mm diameter and data were collected at temperatures of 300 K and 600 K for each sample. The ND patterns were refined with the program Jana2006 using TOF pseudo-Voigt functions with back-to-back exponential functions and using the profile function of POWGEN. The background was interpolated between manually set points. During the final cycles of the refinement, the occupancy factors of Ti and Al were constrained to add up to full occupation. Their thermal displacement and position parameters were constrained to be equal. The thermal displacement parameters (TDP) of Li atoms on Li1 and Li2 sites were also constrained to be equal. The TDP and site occupation factors (SOF) of Li atoms were refined in alternating cycles until convergence was reached ($< 0.1\%$ difference between cycles).

3 Results and Discussion

3.1 Structural Refinements

As discussed in the introduction the structure of LATP is somewhat controversial. In this paper, computational modelling coupled with experimental synthesis and characterisation results will be discussed to address the discrepancies reported in the literature.

The structure refinement based on ND data results in unit cell parameters and distances, especially within the polyanionic framework, that agree well with the results of PB (potentials-based) and DFT calculations, as well as structures published in the literature, see table 2.

Table 2 Lattice parameters (a, b, c) and nearest cation–oxygen interatomic distances are given for structures optimized using the interatomic Buckingham potentials-based (PB) model and DFT (PBE functional). Li1 represents the (M1(6b)) and Li2 is the (M1$'$(6a))[7] or the (M2(18e))^{thiswork} Data obtained from this work are for x=0.3 at 300 K.

	PB model	DFT	Expt.[7]	Expt. (this work)
a (Å)	8.423	8.610	8.511	8.507
b (Å)	8.423	8.610	8.511	8.507
c (Å)	21.613	21.072	20.828	20.833
Al–O (Å)	1.824	1.867	1.883	1.895
Li1–O (Å)	2.259	2.231	2.268	2.270
Li2–O (Å)	1.962	1.955	2.025	1.800
P–O (Å)	1.567	1.537	1.525	1.525
Ti–O (Å)	1.881	1.920	1.883	1.895

When all Li site occupancies are refined, at 300 K, the Li1 site is (almost) fully occupied, and additional Li$^+$ ions are randomly occupying a fraction of the 36f sites. This behavior was also observed by Redhammer *et al.*[15] Occupation of the M1' (6a) site with Li previously found by Dashjav and Tietz could not be observed based on the current data. Upon increasing the temperature to 600 K, the population of Li2(18e) sites increases at the expense of the Li1 sites. The TDP of Li tends to increase with increasing x, but does not change with increasing temperature. This is rather unexpected and, together with the absence of a clear trend in Li distribution, can be attributed to the correlation between SOF and TDP, which cannot be resolved based on ND data.

While ND should in principle be able to determine the position of Li$^+$ ions, the particular case of LATP is rather challenging. The distribution of Li among the different crystallographic sites seems to depend on the preparation route, making it difficult to compare different data sets in the literature and our own experiments. Furthermore, the strong correlation between SOF and TDP makes it difficult to refine either of these parameters accurately. Unfortunately, it is just the combination of these two parameters that reflects the static and dynamic disorder in the LATP structure. Despite these known issues, in this work the positions, SOF, and TDP are refined in order to study the influence of the substitution parameter x and temperature on the distribution of Li$^+$ ions in the structure. Additional structure refinements were carried out where the M1 site is fully occupied as indicated by the MD and DFT calculations. The results are summarized in table 3. Full results of the structure refinement in CIF format are available as supplementary material.

When the SOF of the Li1 site is fixed to full occupation as suggested by MD and DFT calculation (and in agreement with Redhammer *et al.*[15]), the fraction of Li on the 18e or 36f site is given by the chemical composition as described by the substitution parameter x. Again, there is no evidence for Li on the M1$'$ (6a) site. Two refinements were carried out for each composition and temperature, one with Li on the 18e site (Li2) and the other one with Li on the 36f site (Li3). Both refinements in each case result in the same framework structure within the respective standard deviations and provide an equally good fit to the experimental data as indicated by the residuals of the refinement. The resulting TDP are the same with the exception of the data set with $x = 0.4$ at 600 K. However, a large TDP and a split atom position are essentially describing the same type of disorder or dynamics. Therefore, the more symmetric 18e site can be used to describe the average structure in the present case.

Although the structure refinement is able to determine accurate positional parameters especially for the polyanionic framework with good agreement between data presented in this work, literature data, and results from DFT calculations, the distribution and the dynamics of the Li$^+$ ions in the structure remains controversial and to some extent arbitrary depending on the chosen constrained or fixed parameters. This is the point where MD simulations can provide additional insight. The open questions that require a combined experimental/modeling approach are as follows:

- Do the structure models really display the dynamics of Li motion? Is the SOF more than just an occupation probability averaged over the time of the measurement?
- Can a modeling approach give more details on the dynamics and serve as guideline for a better crystallographic model?
- Does a structure model with validated (modelled) input data give better results in terms of goodness of fit and remaining nuclear density?

In order to elucidate the Li$^+$ positions as a function of temperature, MD simulations were setup using the previously reported structure[7] as a guide thereby starting with approximately 0.7 Li1 (6b) and 0.3 Li1 (6a) sites occupied, see figure 3.

Each of the configurations used in this study started with partial occupancy of the M1$'$(6a) sites. It can be seen from figure 3 that as the temperature increases the Li$^+$ ions move from the

Table 3 Site occupation factors of the Li sites and thermal displacement parameter of Li in the crystal structure of LATP determined from ND data. In the case of the refinements with fixed Li site occupancies, extra Li atoms were placed on either the 18e or 36f sites.

	x = 0.3, T = 300 K		x = 0.3, T = 600 K		x = 0.4, T = 300 K		x = 0.4, T = 600 K		x = 0.5, T = 300 K		x = 0.5, T = 600 K	
Site	Refinement including Li site occupancies											
Li1 (6b)	0.98		0.81		0.85		0.70		0.71		0.77	
Li2 (18e)	0.04		0.08		0.09		0.12		0.13		0.12	
TDP (Li)	0.064		0.0663		0.082		0.082		0.110		0.084	
	Refinement with fixed Li site occupancies											
Li1 (6b)	1		1		1		1		1		1	
Li2 (18e)	0	0.1	0	0.1	0	0.133	0	0.133	0	0.167	0	0.167
Li3 (36f)	0.05	0	0.05	0	0.067	0	0.067	0	0.083	0	0.083	0
TDP (Li)	0.085	0.09	0.09	0.09	0.16	0.16	0.08	0.14	0.08	0.08	0.12	0.12

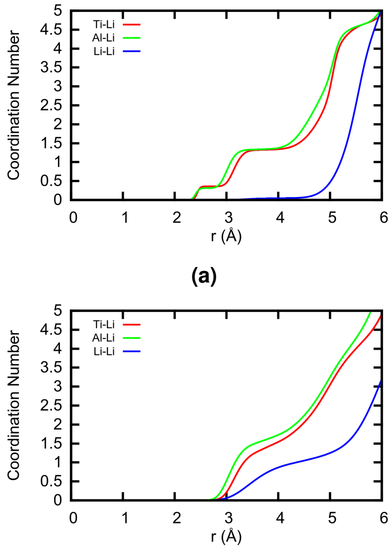

(a)

(b)

Fig. 2 Computed integrated radial distribution functions for Ti–Li, Al–Li and Li–Li coordination a) 273 K and b) 573 K showing the trapping effect of Al on Li.

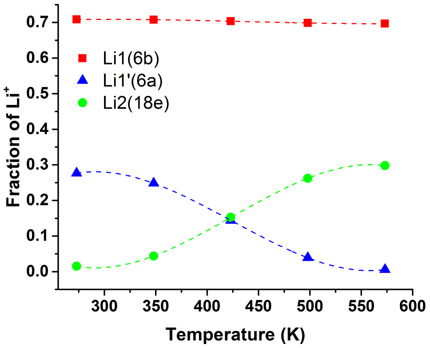

Fig. 3 Computed fraction of Li^+ on the M1(6b), M1′(6a) and M2(18e) sites in LATP as a function of temperature.

M1′(6a) sites to the M2(18e) sites, while the M1(6b) site fractions remain relatively unchanged. For M2(18e) sites, a correlation between occupancy and proximity to Al^{3+} ions is demonstrated in figure 2. M2(18e) sites which are closer to an Al^{3+} ion are likely to have higher occupancies. This agrees with work by Lang *et al.*[8] who showed that Li^+ sites neighbouring Al^{3+} ions are lower in energy than other locations in the unit cell i.e. clustering. This maybe due to a stronger repulsion between Li^+ and Ti^{4+} compared to Li^+ and Al^{3+} ions. We use this data to improve our experimental structural refinements shown in table 3.

The total Li^+ positions from all snapshots during the simulation from the 5×5×2 supercell are superimposed and evaluated. This elucidates the Li ion diffusion pathway (discussed in detail below) but more importantly maps the changes in favoured site occupancies. At low temperatures (273 K), Li^+ density remains primarily on the starting M1(6b) and M1′(6a) sites, see figures 3 and 4. M1(6b) sites present higher occupancies and show wider *a* and *b*-axial vibrational motion than the M1′(6a) sites. At higher temperatures (573 K) however, the connectivity between M1(6b) and M2(18e) sites can be seen (figure 5) and Li^+ migration events involving M1′(6a) sites account for only ∼0.4 % of all observed site-to-site jumps, whereas M1(6b)-M2(18e), M2(18e)-M2(18e) and M1(6b)-M1(6b) site jumps account for around 50, 33 and 16 % of all observed jumps, respectively. The three dimensional network matches images proposed by investigating the Connolly

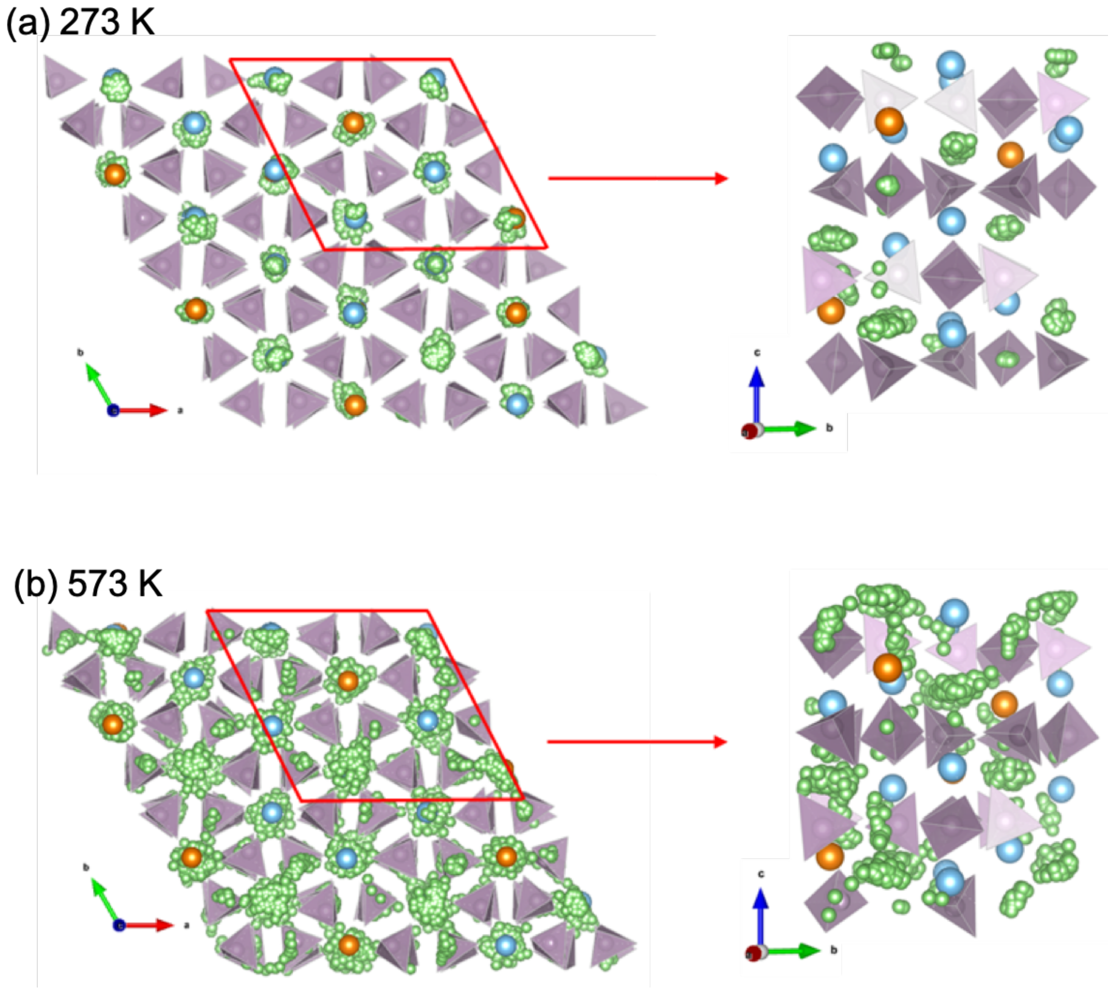

Fig. 4 Computed lithium ion pathways in LATP at a) 273 K and b) 573 K. The Li, Al and Ti sites are shown in green, orange and blue, respectively. The PO_4 tetrahedra are shown in purple. The leftmost picture in a) and b) shows a zoomed out view, to show the scale of the Li^+ diffusion within LATP. The middle and rightmost pictures of a) and b) are zoomed in to the highlighted sections for a more detailed look.

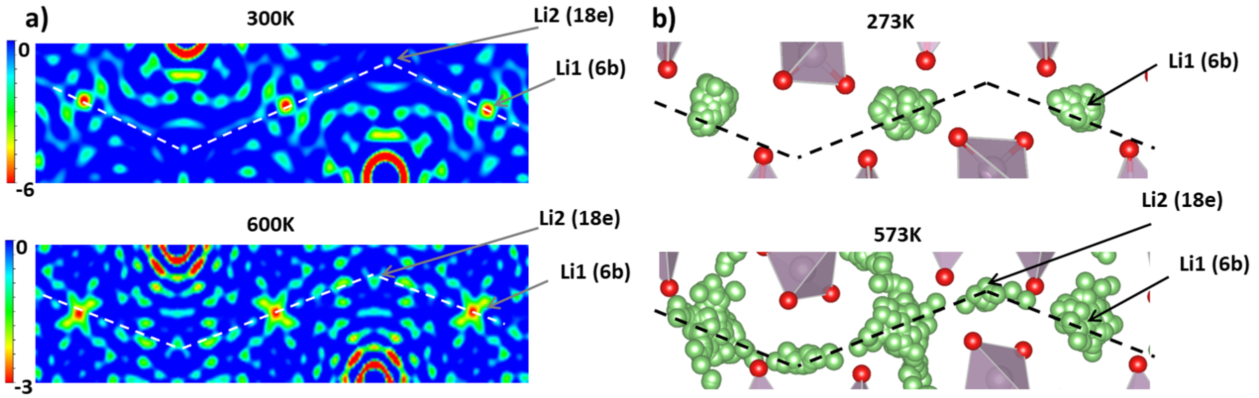

Fig. 5 Lithium ion pathways in LATP. a) shows 2D slices of the observed Fourier map for LATP x=0.4 samples at two different temperatures (300 and 600 K). The Miller indices of this plane are (1 1 4), which goes directly through the Li atoms. The dashed line indicates the linear connection path between the Li1 and Li2 atoms. We can see some Li nuclear density along the dashed lines, which is greater at 600 K than at 300 K. b) shows the corresponding slice taken from molecular dynamics studies, at 273 and 573 K respectively, demonstrating matching Li distributions. Once again, the dashed line indicates the Li diffusion pathway. Li and O atoms are green and red respectively. PO_4 tetrahedra are represented by the purple polyhdedra.

surface (Nuspl *et al.*[17]) and by generating the density from diffraction experiments (Monchak *et al.*[9]), and this study reaffirms that this is the pathway of Li^+ in LATP.

To investigate the energetics of the different lithium sites, *ab initio* calculations were performed and then compared to force field optimisations of the unit cell with displaced lithium atoms. These results, presented in table S5, show that an additional lithium placed at the M2(18e) site in LTP is lower in energy than one placed at the M1′(6a) sites. To investigate the influence of substituting aluminium and lithium for titanium, the composition $Li_{1.17}Al_{0.17}Ti_{1.83}(PO_4)_3$ was defined by creating six cells with M1′(6a) sites occupied and one cell with additional M2(18e) sites occupied. Again, the M2(18e) site is much lower in energy, whether optimised with force field or DFT. While extensive sampling would be required to permit complete analysis, the magnitude of the energy differences engenders confidence in these results as it is far greater than k_bT over the simulated temperature range. These DFT results back up our assertion that lithium will favour M2(18e) sites over M1′(6a) positions. These results also help quantify errors in the force field: energetic ordering trends are maintained, but energy magnitudes are exaggerated by the force fields, with respect to DFT. The Li^+ on the M1’(6a) occupation pattern is unstable, but could be kinetically favoured by certain synthesis conditions perhaps.

3.2 Li ion diffusion

It has been found that Li^+ ion conduction in LATP strongly increases with x up to $x = 0.2$, but does not offer much improvement from 0.3 to 0.5.[10,12,15] It was proposed that this is due to the formation of secondary $AlPO_4$ and $Li_4P_2O_7$ phases at the surface of the LATP particles.[16] As this behaviour will not be encountered in simulations, a x value of 0.4 is therefore selected to ensure sufficient Li^+ ion sampling. There are different Li conduction mechanisms active in a polycrystalline sample: bulk conductivity, grain boundary conductivity, other phases. The present study focuses on bulk conductivity and the underlying conduction pathway. From experimental data, x=0.4 is (close to) the maximum Li content and therefore this concentration was selected for the MD simulations. The higher Li compensating defects also meant that meaningful statistics could be gathered for realistic timescales.

From our MD simulations we confirm that no phase changes are observed during simulation and only the Li^+ ions diffuse, which agrees with the NMR study carried out by Epp *et al.*[4], (see figure S1).

In the NMR study by Epp *et al.*[4] it is suggested that the diffusion data is best fitted by proposing two fast diffusion events, with diffusivity coefficients of 3×10^{-9} cm^2 s^{-1} and 5×10^{-8} cm^2 s^{-1} at room temperature. This again agrees with diffusion coefficient 5.5×10^{-9} cm^2 s^{-1} calculated at 273 K from the MD simulations conducted in this work. The calculated Li^+ ion distribution along the ion pathway is compared to the corresponding distribution derived from ND data in figure 5. Fourier maps clearly show the observed nuclear density at 300 K and 600 K in the $(1\bar{1}\bar{4})$ plane, which contains the Li1 and Li2 positions.The pathway is analysed by looking at the nuclear density figure 5a or snapshots of the Li ion positions from MD, figure 5b. At 300 K, the density around Li1 is smeared from the 6b position. The density peak corresponding to Li2 is weak due to the low population of this site. At 600 K, the smearing of nuclear density around Li1 is more pronounced, the peak intensity at the Li2 site is higher (in agreement with the higher SOF), and the additional density on the dashed line appears. These observations are reflected by the MD results as indicated by the distribution of Li^+ ion positions shown in figure 4-b.

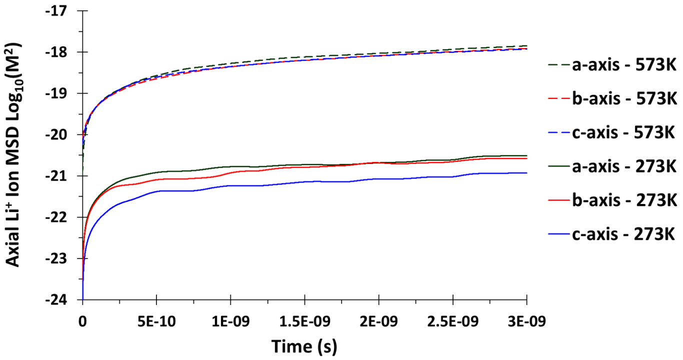

Fig. 6 Li^+ ion axial MSD values averaged over all LATP systems plotted as a function of time. Recorded at 273 K (solid lines) and 573 K (dashed lines).

Table 4 Diffusion coefficients and bulk conductivity for Li^+ ions in LATP as a function of temperature. Bulk conductivity calculated using the Nernst-Einstein equation, $\sigma = DNq^2/fTk_B$, where D is the diffusion coefficient, N is the number of Li ions per m^3, q is the charge on an electron, f is the Haven ratio, T is the temperature and k$_B$ is the Boltzmann constant. The Haven ratio is calculated to be 0.222, based on an average Li^+—Li^+ coordination of 2.57 and the assumption of uncorrelated vacancy site migration, which is likely to be valid at lower temperatures.[33]

Temperature (K)	Diffusion Coefficient cm^2 s^{-1}	Bulk Conductivity S cm^{-1}
273	2.600 x10^{-9}	4.478 x10^{-4}
348	1.950 x10^{-8}	2.635 x10^{-3}
423	1.478 x10^{-7}	1.643 x10^{-2}
498	7.858 x10^{-7}	7.420 x10^{-2}
573	1.715 x10^{-6}	1.408 x10^{-1}

Axial mean squared displacements for Li^+ ions in LATP at 273 and 573 K are plotted in figure 6. At low temperatures ion transport in the a and b axial components are more dominant, which is consistent with the asymmetry in the lithium density at the M1(6b) sites, see figure 4-a. At higher temperatures, c-axial diffusion becomes more dominant, at which point the diffusion coefficient increases linearly with temperature, as shown in figure 7. From the Arrhenius equation, an activation energy of 0.303 eV is calculated, which agrees with the experimentally calculated values of 0.282 eV[34] and 0.330 eV.[9,35]. If we calculate the ionic conductivities, see table 4, we do get ionic conductivities that are comparable to experimental bulk measurements giving further confidence in our computational models and hence the interesting results presented above.

4 Conclusions

This paper presents a collaborative and systematic study to highlight the sensitivities of synthesising LATP and correlating this to observed properties. Computationally, an interatomic potential model for $Li_{1+x}Al_xTi_{2-x}(PO_4)_3$ has been refined to represent the experimental crystal structural properties and the x=0.4 composition has been studied using molecular dynamics to sample Li^+ ion diffusion in the material. The pathway reported here, *via* the M2(18e) sites, is the same as has been experimentally observed by others.[9] In the best fit to neutron diffraction data reported by Dashjav and Tietz,[7] it was proposed that Li^+ ions inhabit the M1′(6a) sites. However, the molecular dynamic studies undertaken here suggest that these sites are unfavourable, a proposal which is reaffirmed through DFT calculations, but highlighting the sensitivity of diffusivity with synthesis conditions.

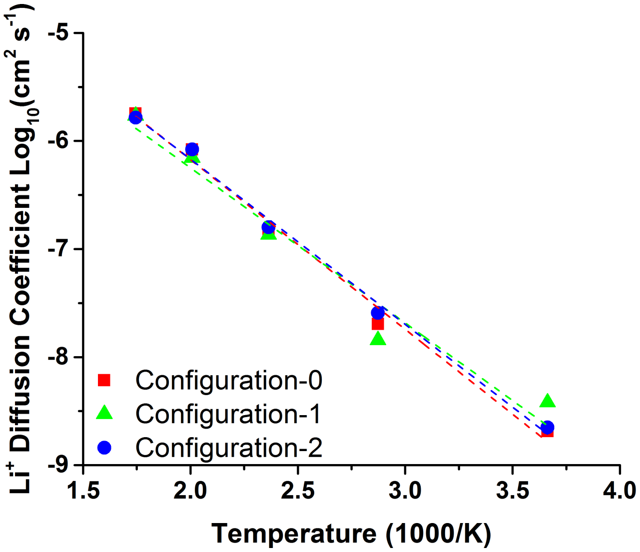

Fig. 7 Diffusion coefficients for Li^+ ions in LATP as a function of temperature. Individual datasets for each configuration have been given in the supplementary information.

The experimental data shown in this work give no evidence for Li on the M1(6a) site, in agreement with the DFT calculations, in contrast to the results given by Dashjav and Tietz.[7] The reason strongly points towards the different preparation route, where the high temperature solid state reaction may result in reaction products that are not in thermodynamic equilibrium. The low temperature route used in this work results in a distribution of Li^+ ions that is found to be energetically favourable by DFT calculations.

This is a significant finding, particularly when scaling up the manufacture of such solid-state materials for battery applications. Given that a wide range of high temperature procedures are available to the synthetic materials scientist, a wide range of possible atomic configurations may be synthesized, and these must be considered when searching for diffusion pathways. This study is the first to take a starting configuration in which the M1′(6a) sites are occupied. However, the initial occupation of these sites was not observed to cause a significant deviation from the M1(6b)-M2(18e)-M1(6b) pathway. Furthermore, the system relaxed during the course of the simulation, and then recovered behaviour which was seen to closely match experimental data, such as diffusion constants, activation barriers, and statistical relationships with respect to substitution of titanium for aluminium.

5 Acknowledgements

The authors acknowledge several INNOVATE–UK grants, **(TS/N00941X/1)**, Solid INTERface Batteries: SINTER and **(TS/R002312/1)**, Practical and Robust Lithium Air Batteries: PROLAB. PG and SRY also acknowledge the support of EPSRC SUPERGEN grant, **EP/N001982/1**. The authors are grateful for the use of the 'Hydra' High Performance System at Loughborough University. *Via* our membership of the UK's HEC Materials Chemistry Consortium, which is funded by EPSRC **(EP/L000202, EP/R029431)**, this work used the ARCHER UK National Supercomputing Service (http://www.archer.ac.uk). We strongly acknowledge the use of Athena as part of the HPC Midlands+ consortium, funded by the EPSRC on grant **EP/P020232/1**. The authors gratefully acknowledge the financial support provided by JCNS to perform the neutron scattering measurements at the Spallation Neutron Source (SNS), Oak Ridge, USA. Part of this research used resources at the Spallation Neutron Source, a Department of Energy Office of Science User Facility operated by Oak Ridge National Laboratory.

References

1 Z. Xiao, M. Ma and X. Wu, *Trans. Nonferrous Met. Soc. China*, 2006, **16**, 281.

2 S. J. Visco, V. Y. Nimon, A. Petrov, K. Pridatko, N. Goncharenko, E. Nimon, L. De Jonghe, Y. M. Volfkovich and D. A. Bograchev, *J. Solid State Electrochem.*, 2014, **18**, 1443–1456.

3 S. Duluard, A. Paillassa, P. Lenormand, P.-L. Taberna, P. Simon, P. Rozier and F. Ansart, *J. Am. Ceram. Soc.*, 2017, **100**, 141–149.

4 V. Epp, Q. Ma, E.-M. Hammer, F. Tietz and M. Wilkening, *Phys. Chem. Chem. Phys.*, 2015, **17**, 32115–32121.

5 W. Ślubowska, K. Kwatek, C. Jastrzębski and J. L. Nowiński, *Solid State Ionics*, 2019, **335**, 129 – 134.

6 G. Yan, S. Yu, J. F. Nonemacher, H. Tempel, H. Kungl, J. Malzbender, R.-A. Eichel and M. Krüger, *Ceramics International*, 2019.

7 E. Dashjav and F. Tietz, *Zeitschrift für Anorg. und Allg. Chemie*, 2014, **640**, 3070–3073.

8 B. Lang, B. Ziebarth and C. Elsässer, *Chem. Mater.*, 2015, **27**, 5040–5048.

9 M. Monchak, T. Hupfer, A. Senyshyn, H. Boysen, D. Chernyshov, T. Hansen, K. G. Schell, E. C. Bucharsky, M. J. Hoffmann and H. Ehrenberg, *Inorg. Chem.*, 2016, **55**, 2941–2945.

10 K. Arbi, M. Hoelzel, A. Kuhn, F. Garcia-Alvarado and J. Sanz, *Phys. Chem. Chem. Phys.*, 2014, **16**, 18397–18405.

11 H. Aono, E. Sugimoto, Y. Sadaoka, N. Imanaka and G. Adachi, *J. Electrochem. Soc.*, 1989, **136**, 590–591.

12 Q. Ma, Q. Xu, C. Tsai, F. Tietz and O. Guillon, *J. Am. Ceram. Soc*, 2016, **99**, 410–414.

13 Z. Li and X. Zhao, *Functional Materials Letters*, 2019.

14 M. Kotobuki and M. Koishi, *Journal of Asian Ceramic Societies*, 2019, **7**, 69–74.

15 D. Rettenwander, A. Welzl, S. Pristat, F. Tietz, S. Taibl, G. Redhammer and J. Fleig, *J. Mater. Chem. A*, 2016, **4**, 1506–1513.

16 K. Arbi, J. M. Rojo, J. Sanz, J. M. R. K. Arbi and J. Sanz, *J. Eur. Ceram. Soc.*, 2007, **27**, 4215–4218.

17 G. Nuspl, T. Takeuchi, A. Weiß, H. Kageyama, K. Yoshizawa and T. Yamabe, *J. Appl. Phys.*, 1999, **86**, 5484–5491.

18 R. A. Buckingham, *Proc. R. Soc. A Math. Phys. Eng. Sci.*, 1938, **168**, 264–283.

19 B. G. Dick and A. W. Overhauser, *Phys. Rev.*, 1958, **112**, 90–103.

20 J. D. Gale, *J. Chem. Soc. Faraday Trans.*, 1997, **93**, 629–637.

21 J. D. Gale and a. L. Rohl, *Mol. Simul.*, 2003, **29**, 291–341.

22 M. S. Islam, D. J. Driscoll, C. A. J. Fisher and P. R. Slater, *Chem. Mater.*, 2005, **17**, 5085–5092.

23 A. K. Padhi, K. S. Nanjundaswamy and J. B. Goodenough, *J. Electrochem. Soc.*, 1997, **144**, 1188–1194.

24 I. M. Sobol, *U.S.S.R Comput. Maths. Math. Phys.*, 1967, **7**, 86–112.

25 A. Aatiq, M. Ménétrier, L. Croguennec, E. Suard and C. Delmas, *J. Mater. Chem.*, 2002, **12**, 2971–2978.

26 R. Skala, D. Li and I. Low, *J. Eur. Ceram. Soc*, 2009, **29**, 67–75.

27 G. Kresse and J. Hafner, *Phys. Rev. B*, 1993, **47**, 558–561.

28 O. Dolotko, A. Senyshyn, M. J. Mühlbauer, H. Boysen, M. Monchak and H. Ehrenberg, *Solid State Sci.*, 2014, **36**, 101–106.

29 W. Smith and T. R. Forester, *J. Mol. Graph.*, 1996, **14**, 136–141.

30 S. Ong, Y. Mo, W. Richards, L. Miara, L. H.S. and G. Ceder, *Energy Environ. Sci.*, 2013, **6**, 148–156.

31 F. Pedregosa, G. Varoquaux, A. Gramfort, V. Michel, B. Thirion, O. Grisel, M. Blondel, P. Prettenhofer, R. Weiss, V. Dubourg, J. Vanderplas, A. Passos, D. Cournapeau, M. Brucher, M. Perrot and E. Duchesnay, *Journal of Machine Learning Research*, 2011, **12**, 2825–2830.

32 Q. Ma, F. Tietz and O. Guillon, 2014, German patent, DE 10 2014 012 926.

33 J. Isard, *Journal of non-crystalline solids*, 1999, **246**, 16–26.

34 Z.-b. Xiao, S. Chen and M.-m. Guo, *Trans. Nonferrous Met. Soc. China*, 2011, **21**, 2454–2458.

35 E. Dashjav, Q. Ma, Q. Xu, C.-L. Long, M. Giarola, G. Mariotto and F. Tietz, *Solid State Ionics*, 2018, **321**, 83–90.